Nuclear Materials and Energy 20 (2019) 100676

Contents lists available at ScienceDirect

Nuclear Materials and Energy

journal homepage: www.elsevier.com/locate/nme

Spectroscopic investigation of N and Ne seeded induced detachment in JET ITER-like wall L-modes combining experiment and EDGE2D modeling

B. Lomanowski[a,c,*], M. Carr[b], A. Field[b], M. Groth[c], A.E. Jaervinen[d], C. Lowry[e,f], A.G. Meigs[b], S. Menmuir[b], M. O'Mullane[g], M.L. Reinke[a], C.K. Stavrou[h], S. Wiesen[i], JET contributors[1]

[a] Oak Ridge National Laboratory, Oak Ridge, TN 37831, USA
[b] CCFE, Culham Science Centre, Abingdon, OX14 3DB, UK
[c] Aalto University, Espoo, Finland
[d] Lawrence Livermore National Laboratory, Livermore, USA
[e] European Commission, Brussels, Belgium
[f] JET Exploitation Unit, Culham Science Centre, Culham, OX14 3DB, UK
[g] Department of Physics, University of Strathclyde, Glasgow G4 0NG, UK
[h] Tokamak Energy Ltd, 173 Brook Drive, Milton Park, Abingdon OX14 4SD, UK
[i] Forschungszentrum Jülich GmbH, Institut für Energie-und Klimaforschung-Plasmaphysik, 52425 Jülich, Germany

ARTICLE INFO

Keywords:
Impurity seeded detachment
Divertor spectroscopy
Detachment evolution
JET-ILW
EDGE2D-EIRENE

ABSTRACT

Modeling and experimental investigation of the distribution of seeded impurities and their influence on divertor detachment in all-metal tokamaks is critical for developing reactor-scale exhaust scenarios. In this work, the degree and operating space for Ne and N impurity seeded induced detachment in JET with ITER-like wall (JET-ILW) L-mode discharges is shown to be regulated by the combination of i) the local radiative dissipation in the low-field side divertor; and ii) the incursion of the ionization front towards the X-point with increased impurity seeding. Using a quantitative spectroscopic approach, it is shown that the net particle balance at the low-field side target is dominated by a marked decrease in the ionization source between the X-point and the target with increased N and Ne seeding, and only a marginal increase in the volume recombination rate. With increased seeding, the local radiated power dissipation (N only) and reduction in the power crossing the separatrix (both nitrogen and neon) leads to a reduction in the low-field side target T_e. Consequently, the incursion of the ionization front away from a region of enhanced ionization rate caused by high Lyman series opacity at the outer target leads to a steep decrease of the outer target ion flux. In contrast to experiment, EDGE2D-EIRENE simulations using optically thin divertor plasma assumptions show a larger impact of volume recombination and a factor of two shortfall in the low-field side divertor n_e. A detailed assessment of opacity effects using the EIRENE photon transport module is recommended.

1. Introduction

Mitigation of the large heat fluxes convected to divertor targets of future reactor-scale tokamaks via a thin (~ few mm) channel in the scrape-off layer (SOL) will require radiative dissipation of most of the exhaust power in order to spread the concentrated heat flux over a larger area. For ITER and DEMO, where 85–90%, and more than 95% of the exhaust power needs to be dissipated [1,2], respectively, the most viable solution involves seeding of impurities which can radiate a major fraction of the heat flux via line radiation.

High radiation scenarios at a high ratio of the power flux crossing the separatrix over the major radius, P_{sep}/R (the main parameter determining the heat flux), have recently been demonstrated [3–6] on ASDEX-Upgrade (AUG) ($P_{sep}/R \approx 10$–12 MW m^{-1}) and JET with the ITER-like wall (JET-ILW) ($P_{sep}/R \approx 5$ MW m^{-1}) using seeding impurities including nitrogen (N) and neon (Ne). While N seeding has been shown to increase energy confinement [7] as well as to increase radiation in the divertor, achieving stable discharges with Ne seeding has proven to be generally more challenging on metal wall devices [3], in contrast to previous studies on carbon walled machines (e.g., [8,9]). Ne seeding in high-confinement mode (H-mode) on AUG and JET-ILW typically leads to core impurity accumulation caused by the

* Corresponding author.
E-mail address: lomanowskiba@ornl.gov (B. Lomanowski).
[1] See the author list of "Overview of the JET results in support to ITER" by X. Litaudon et al. 2017 *Nucl. Fusion* 57 102,001.

https://doi.org/10.1016/j.nme.2019.100676
Received 12 August 2018; Received in revised form 31 March 2019; Accepted 15 April 2019
Available online 16 April 2019

combination of increased neoclassical inward transport and reduced ELM flushing, leading to H-L back-transitions and eventual collapse of the discharge [3]. On both machines a transition from partial to more pronounced detachment at high N seeding is accompanied by the formation of a stable and strongly radiating region inside the X-point, which has not been observed for the Ne cases.

To complement ongoing studies on highly radiative scenarios with impurity seeding, the focus of this paper is on advancing understanding of the dominant mechanisms driving detachment under high-recycling divertor conditions with N and Ne seeding. The analysis relies heavily on the detailed interpretation of spectroscopic measurements, and hence motivates selection of a low-confinement (L-mode) scenario ($P_{sep}/R \approx 1$ MW m^{-1}) in a diagnostically optimized outer horizontal target configuration to maximize the fidelity of the ELM-free discharges and diagnostic data quality.

In high-recycling divertor conditions in which the recycling of neutrals dominates the particle balance at the targets, the basic description of the driving terms regulating the power flow to the target, $P_{plate} = I_{div}(\gamma T_e + \varepsilon)$ can be described using the 'closed box' approximation [10], such that, for low target $T_e \sim 1$ eV,

$$I_{div} = S_{iz} - S_{rec} = \frac{P_{SOL} - P_{rad,Z}}{E_{iz}} - S_{rec} \quad (1)$$

where γ is the sheath heat transmission coefficient, I_{div} is the total ion flux to the target in #/s, ε is the deuterium ionization potential (13.6 eV), S_{iz} and S_{rec} are the total ionization and recombination rates in the plasma volume near the targets, P_{SOL} is the power flow in the SOL, $P_{rad,Z}$ the impurity radiated power and E_{iz} the 'ionization cost' which relates the power loss associated with the deuterium ionization process to the ionization rate, $P_{iz} = E_{iz}S_{iz}$. According to this description, for a given P_{SOL}, the reduction of the plasma flux to the target can be achieved mainly through impurity radiation and/or volume recombination, assuming $E_{iz} \sim 30$ eV is approximately constant. The aim of the study is to quantify the I_{div} reduction mechanisms using a suite of bolometry and spectroscopic measurements that are also consistently applied to post-processing the numerical results. No attempt is made to extrapolate the results to higher P_{sep}/R scenarios at present. Rather, the emphasis is placed on assessing any discrepancies and identifying missing physics components in the fluid-neutral codes as part of a validation effort towards refining their predictive capability.

2. Methodology

2.1. Experiment setup

L-mode JET-ILW discharges (P_{NBI} =1.8 MW, I_p = 2.5 MA, B_t = 2.5 T) were carried out in the inner vertical, outer horizontal target configuration (V-T5), shown in Fig. 1. For the reference unseeded case, a high-recycling divertor operational point was selected with feedback control on the line-averaged edge electron density using divertor D_2 fueling such that the ion flux integrated over the outer target, $I_{div,OT}$, was maintained at the roll-over point. A seeding scan with Ne and N was then carried out with successively increasing gas injection rates using a toroidally distributed gas injection module in the outer common SOL (Fig. 1).

2.2. Analysis techniques

An integrated analysis and modeling strategy was developed, combining multiple diagnostic outputs with EDGE2D-EIRENE [11–13] simulations with emphasis on using synthetic observables for direct comparison with experiment.

2.2.1. Spectroscopic estimates of atomic ionization and recombination rates

Outer target radial profiles estimates of n_e from D_δ ($n = 6 \rightarrow 2$) Stark

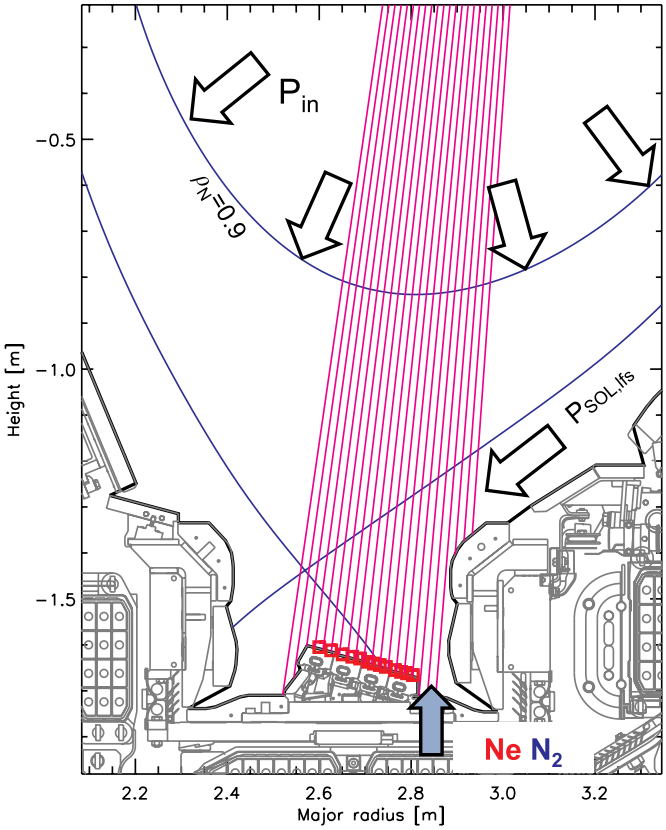

Fig. 1. JET-ILW V-T5 plasma configuration with outer divertor visible spectroscopy chords (magenta) and Langmuir probe locations on tile 5 (red); definition of the input power P_{in} into the EDGE2D-EIRENE computational domain; total power flow to the outer divertor SOL $P_{SOL,lfs}$; and the seeding injection location. (For interpretation of the references to color in this figure legend, the reader is referred to the web version of this article.)

broadening [14] and T_e from the Balmer photo-recombination continuum emission [14,15] measured by the vertically viewing divertor visible spectroscopy system [16,17] (Fig. 1) were used as constraints for estimates of the plasma ion source (i.e., ionization of D atoms) and sinks (i.e., volume recombination of D^+ ions, including direct and three-body reactions) using ADAS [18] inverse photon efficiency coefficients. Corresponding radial profiles of Ly_α intensity, $I_{2\text{-}1}$, measured by the scanning mirror vacuum-ultraviolet spectrometer [19] were used for the ionization estimates

$$S_{iz} = 4\pi I_{2\rightarrow1}\frac{SCD(T_e, n_e)}{PEC^{exc}_{2\rightarrow1}(T_e, n_e)} \quad (2)$$

where *SCD* and *PEC* are ADAS effective ionization and photon emissivity coefficients, respectively, and $I_{2\text{-}1}$ is assumed to be excitation dominated. An assessment of the contributions to $I_{2\text{-}1}$ from different atomic and molecular collisional channels using the diagnostic output from the EIRENE [20] kinetic neutral transport model showed that electron excitation from the ground state dominates over direct and three body recombination . A high recycling EDGE2D plasma solution was used for the EIRENE assessment, with the model set up as described in Section 2.3. The EIRENE results also showed negligible contributions from molecular excitation channels, which include dissociative excitation from D_2 and mutual neutralization with D^-, while dissociative recombination from $D_2{}^+$added a modest contribution outboard of the outer strike point (OSP) where $I_{2\text{-}1}$ is low (see for example [21] for more details on atomic-molecular population modeling). On the other hand, for the same background plasma, population contributions to D_α emission, $I_{3\text{-}2}$, included a significant component from $D_2{}^+$ dissociative recombination [22]. The assessment is consistent with previous studies

[23,24] on the contribution to deuterium Lyman and Balmer series emission from molecular-plasma interactions in tokamak divertors.

The volume recombination rate was calculated using the D_ε intensity $I_{7\text{-}2}$:

$$S_{\text{rec}} = 4\pi I_{7\to 2}\frac{ACD(T_e, n_e)}{PEC^{\text{rec}}_{7\to 2}(T_e, n_e)} \quad (3)$$

where *ACD* is the ADAS effective recombination coefficient and the $n = 7$ population is assumed to be dominated by direct and three-body recombination contributions, generally valid for $T_e \leq 2$ eV, and is free of molecular excitation channel contributions. The magnitude of the recombination contributions to $I_{2\text{-}1}$, $I_{3\text{-}2}$ and $I_{7\text{-}2}$ is further assessed in spectroscopic post-processing of the simulation results in Section 4.

2.2.2. Lyman series opacity

Measurements of the $(I_{3\text{-}1}/I_{3\text{-}2})(A_{3\text{-}2}/A_{3\text{-}1})$ line ratio at and outboard of the outer strike point in the unseeded reference show a significant reduction in the ratio below the optically thin 1:1 value with increasing fueling. $A_{3\text{-}2}$ and $A_{3\text{-}1}$ are the spontaneous emission rates from the $n = 3$ excited level. The modification of the $(I_{3\text{-}1}/I_{3\text{-}2})(A_{3\text{-}2}/A_{3\text{-}1})$ ratio with neutral density is not dependent on the details of the population contributions for $n = 3$, and is therefore considered to be the most direct measure of divertor opacity (see [25] for an overview of radiation transport in the tokamak context). These measurements suggest that the divertor plasma at and outboard of the OSP is optically thick, and hence the neutral density n_D is sufficiently high to cause Ly-series reabsorption (opacity $\tau = L/\lambda_{\text{mfp}} \propto Ln_D$, where L is the characteristic size of the emitting region and λ_{mfp} is the photon mean free path).

Following [26,27], a more useful measure of the degree of opacity can be obtained using the population escape factor $\Theta_{i\text{-}j}$ for a radiative transition from level i to j, defined as the probability of photon escape along a line-of-sight (i.e., $\Theta_{i\text{-}j} = 1$ in optically thin plasma, $\Theta_{i\text{-}j} = 0$ for full reabsorption). The Ly_β escape factor, $\Theta_{3\text{-}1} = (I_{3\text{-}1}/I_{3\text{-}2})(A_{3\text{-}2}/A_{3\text{-}1})$, which is measured directly, serves as the basis for estimating escape factors for other Lyman transitions, as in [27]. In the L-mode high-recycling conditions, $\Theta_{3\text{-}1}$ and $\Theta_{2\text{-}1}$ outboard of the OSP ere estimated to be at or below 0.4 and 0.1, respectively.

Radial profiles of S_{iz} and S_{rec} from line-integrated spectroscopy can be corrected for opacity by using a modified ADAS data set where $A_{i\text{-}j}$ is replaced with $A_{i\text{-}j,\text{eff}} = \Theta_{i\text{-}j}A_{i\text{-}j}$ for the Ly series up to $n = 5$, which yields modified *SCD, ACD* and *PEC* coefficients to be used in Eqs. (2) and (3). The implicit assumption in using the effective spontaneous emission rates is isotropic emission corresponding to a 0-D approximation along the line-of-sight of each spectral chord intersecting the outer target. In other words, the details of the spatial emission profiles along each line-of-sight are ignored, although the radial variation in $\Theta_{i\text{-}j}$ along the target is resolved. Likewise, differences in the emitter and absorber spectral line-shapes are also not captured in the population escape factor model. It should be stressed that opacity corrections to atomic rate coefficients used for interpreting spectroscopic measurements do not provide any indication on the impact of opacity on diveror plasma parameters and dynamics, for which more sophisticated radiation transport modeling is required. Full details on the interpretation of opacity measurements in JET-ILW, atomic data corrections and the empirically derived Ly series intensity calibration will be provided in a forthcoming publication.

2.3. EDGE2D-EIRENE simulation setup

EDGE2D-EIRENE simulations were configured with emphasis on matching the plasma conditions upstream at the outer mid-plane as well as in the outer divertor for unseeded conditions. The upstream outer mid-plane n_e and T_e profiles from high-resolution Thomson scattering (HRTS) and lithium-beam measurements (Fig. 2) were used to estimate the outer mid-plane separatrix density within the range

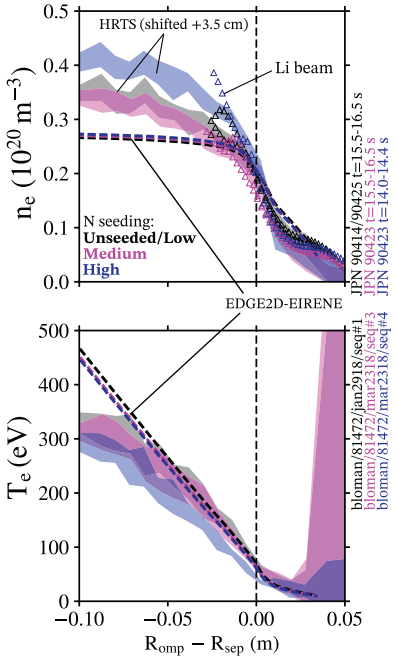

Fig. 2. Outer mid-plane profiles of n_e and T_e from EDGE2D-EIRENE (dashed lines) and experiment high-resolution Thomson scattering (shaded profiles) and lithium beam (triangles) diagnostics. Colors indicate unseeded/low seeding (black), medium (magenta) and high (blue) seeding cases. (For interpretation of the references to color in this figure legend, the reader is referred to the web version of this article.)

$2.0 \times 10^{19} < n_{e,\text{sep}} < 2.2 \times 10^{19}\, m^{-3}$ to account for the uncertainty in the separatrix location in experiment. In the simulations $n_{e,\text{sep}}$ was held constant with D_2 fueling feedback control, following the same control scheme used in experiment. Following the simulation setup in [28] for the upstream transport coefficients (i.e., radial thermal diffusivities $\chi_{i,e} = 0.5$ m^2 s^{-1} and particle diffusivity $D_\perp = 1$ m^2 s^{-1} in the SOL), $D_\perp$ in the SOL below the X-point was reduced to 0.5 m^2 s^{-1} to obtain a better match to the Langmuir probe profiles (see Fig. 5.c).

The input power, P_{in}, to the EDGE2D-EIRENE computational domain, which begins at the edge of the confined core plasma where $\sqrt{\psi_N} = \rho_N = 0.9$, was estimated from experiment from the steady-state power balance $P_{\text{in}} = P_{\text{Ohm}} + P_{\text{NBI}} - P_{\text{rad},\rho N<0.9}$, where $P_{\text{rad},\rho N<0.9}$ was estimated from bolometric reconstructions. Although in experiment $P_{\text{in}} \approx 3.2$ MW, a lower and upper value of $P_{\text{in}} = 3.2$ MW and $P_{\text{in}} = 3.8$ MW was used in the simulation data set to account for the uncertainty in the amount of the power crossing the separatrix, P_{sep}, lost to the main chamber wall. It was found in simulations that about 30% of P_{sep} was consistently lost to the main chamber, whereas thermocouple-based estimates of the power flux to the wall from experiment suggest only about ~5% of P_{sep} [28]. In EDGE2D-EIRENE the SOL thickness is limited due to grid geometry constraints, and hence only extends about 3 cm radially beyond the separatrix at the outer-mid plane. To compensate for this, a SOL wall temperature drop paramter can be used to modify the outer edge boundary condition, but it was found that increasing P_{in} to 3.8 MW instead could be used more reliably to ensure that the power flow to the outer divertor was not significantly underestimated.

As in experiment, an N and Ne seeding scan was carried out in EDGE2D-ERIENE while maintaining constant $n_{e,\text{sep}}$, constant transport coefficients with equivalent $D_\perp$ for both impurities and main ion species, and assuming that N and Ne are fully recycling species. The scans with the upper and lower values of $n_{e,\text{sep}}$ and P_{in} produce some scatter in the data set, but have little impact on the general trends identified in the discussion.

The procedure for inferring S_{iz} and S_{rec} spectroscopically was

replicated in post-processing of EDGE2D-EIRENE simulations using a parameterized Stark broadening line profile model [14] and the adas-slib/continuo Bremsstrahlung model [29] to synthesize the line-integrated spectra. Since the molecular contribution to the $n = 2$ and $n = 7$ populations can be neglected, ADAS *PECs* were used to calculate $I_{2\rightarrow1}$ and $I_{7\rightarrow2}$. Both atomic and molecular plasma interactions were captured in the EDGE2D-EIRENE simulations using and extended set of reaction cards as describe in [30]. For consistency with post-processing, the atom-plasma reaction cards were configured specifically for reading ADAS ionization and recombination rate coefficients instead of the default AMJUEL rates [20], with negligible impact on the plasma solution. The molecule-plasma reaction cards were configured with the default AMJUEL rates.

Although the experiment results suggest that opacity effects may be significant (see Section 4), the EIRENE photon transport module [31] was not available for this study, as development work is ongoing in updating the module in the newest EIRENE version. Hence, Ly series photon reabsorption, and its effects on the plasma solution, are not captured in the modeling.

Interpretation of spectroscopic measurements in the JET-ILW divertor is influenced by reflections since the vertically viewing spectrometer chords intersect the bulk tungsten outer horizontal target (tile 5). The magnitude of the reflected component depends on the divertor strike-point configuration, as well as the inner to outer target emission intensity ratio. Using a sophisticated ray tracing code (RAYSECT/CHERAB) [32,33], and a representative EDGE2D-EIRENE high-recycling plasma solution, the impact on the synthetically derived n_e profile from D_δ Stark broadening was shown to be small, while a large discrepancy was observed in the spectroscopically derived T_e profiles with and without reflections. T_e estimates are inversely proportional to the photo-recombination edge emission at the Balmer series limit, hence regions of high T_e are influenced by the more intense emission from regions of low T_e. The overall effect underestimates T_e inboard of the OSP, while only a modest impact is observed at the OSP, as shown in Fig. 3. All synthetic spectroscopy signals for n_e and T_e estimates were post-processed using RAYSECT/CHERAB for consistency with measurements.

2.3.1. Influence of drift terms

Activation of drift terms in edge fluid simulation packages can significantly influence asymmetries in the divertor power and particle exhaust characteristics (e.g., [34,35]). With the ion $B \times \nabla B$ direction into the divertor poloidal temperature gradients near divertor targets give rise to radial $E_\theta \times B$ drifts which carry particles from outer to inner target through the private flux region and lead to shifts in radial target profiles. In the present study only the unseeded and low N-seeded EDGE2D-EIRENE simulations successfully converged with the poloidal and radial drift terms activated, whereas cases with drifts and with appreciable seeding rates proved to be numerically unstable. As a result, drifts were not included in the simulation data set used for comparison against experiment discussed in the following sections.

From the available low N-seeding ($P_{rad,N} = 0.05$ MW) converged cases with drifts activated, the influence of the drift terms on the divertor solution is shown in the comparison of synthetic spectroscopy radial n_e and T_e profiles in Fig. 3 using a vertical view geometry of the entire divertor. For the same $n_{e,sep} = 2.0 \times 10^{19}\ m^{-3}$, activation of drifts leads to a factor of two increase in n_e and decrease in T_e at the outer and inner targets. The outer target fraction of the total divertor ion current $I_{div,OT}/I_{div,tot}$ decreases from 0.57 to 0.5 while $I_{div,IT}/I_{div,total}$ increases from 0.43 to 0.5. By reducing $n_{e,sep}$ to $1.8 \times 10^{19}\ m^{-3}$ a good match to the outer target profiles in the no-drifts case can be obtained, albeit with a narrower target n_e profile, while the inner target remains denser and cooler compared to the no-drifts case. Hence, while drifts clearly influence the entire divertor solution, it is possible in the context of the present study to compensate for not including drifts to the extent of matching outer target T_e and n_e profiles via a modest ($\sim$10%) change in $n_{e,sep,}$ which is still within the upstream kinetic profile uncertainty in the separatrix location. This is also corroborated by comparing synthetic radial profiles of N II, N III and N IV line emission (Fig. 3). The outer target nitrogen emission profiles from the drifts case with reduced $n_{e,sep}$ are in good agreement with the no-drifts case at higher $n_{e,sep,omp}$. For the low N-seeding cases, the comparison with and without drifts indicates that nitrogen line emission, and thus $P_{rad,N}$, is primarily dependent on the drifts influence on n_e and T_e, rather than direct modification of the impurity transport. This suggests that while the inner divertor is strongly influenced by drifts, it is still possible to examine the well diagnosed outer divertor in isolation without drifts, while acknowledging that at high enough seeding levels drifts are likely to modify the radiation pattern, as shown in [34].

3. Impurity radiation distribution

$P_{rad} = P_{rad,Z} + P_{rad,D}$ is defined as the total radiated power combining the edge confined region, inner and outer SOL, outer divertor and private flux region, but for the purpose of code comparison excludes i) the core region up to $\rho_N = 0.9$ for consistency with the EDGE2D-EIRENE computational domain; and ii) the inner divertor region since drifts were not included in the seeding scan but have a large influence on the inner divertor plasma solution. In the high-recycling conditions examined, the absence of N II line radiation in filtered

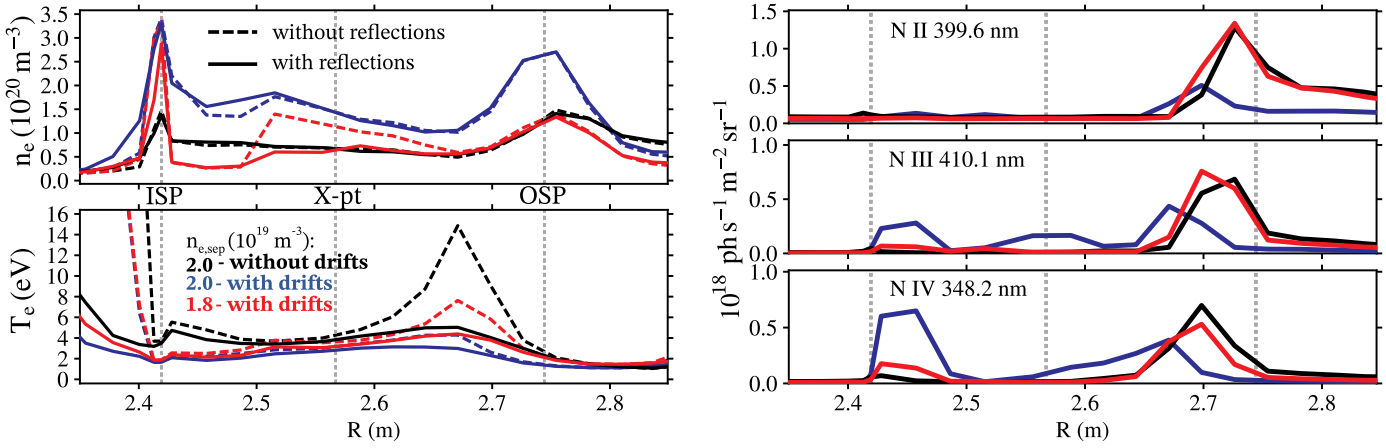

Fig. 3. Synthetic spectroscopy profiles of n_e and T_e (left) and nitrogen line intensities (right) corresponding to simulation cases with $n_{e,sep}$ values of $2.0 \times 10^{19}\ m^{-3}$ without drifts (black), $2.0 \times 10^{19}\ m^{-3}$ with drifts (blue) and $1.8 \times 10^{19}\ m^{-3}$ with drifts (red). (For interpretation of the references to color in this figure legend, the reader is referred to the web version of this article.)

imaging reconstructions in the inner divertor indicates low T_e (< 3 eV) and is consistent with bolometry results which show virtually no impact of Ne or N seeding on the inner divertor radiation. Hence, excluding the inner divertor region from P_{rad} allows for a more meaningful comparison of the impurity radiated fraction in the well diagnosed outer divertor region.

Estimates of $P_{rad,Z}$ for N ($P_{rad,N}$) and Ne ($P_{rad,Ne}$) are obtained from bolometry tomographic reconstructions by subtracting the unseeded reference case radiation $P_{rad,D,ref}$ such that $P_{rad,Z} \approx P_{rad} - P_{rad,D,ref}$ is spatially resolved for each macro region. In the unseeded reference case, approximately 70% of $P_{rad,D,ref}$ in the divertor below $Z = -1.2$ m is accounted for by summing Ly_α, Ly_β, D_α and the free-bound Bremsstrahlung radiation component, leaving about 0.25 MW unaccounted for in the confined X-point region. The core Z_{eff} estimates of 1.0 and 1.3 from mid-plane horizontal and outer vertical chords, respectively, suggest that additional intrinsic impurity radiation could account for the remaining 0.25 MW, or ~10% of P_{in}. Without the benefit of additional information, it is assumed for the present study that $P_{rad,D,ref}$ is approximately constant throughout the Ne and N seeding scan.

Fig. 4 shows estimates of the Ne and N radiation contribution, $f_Z = P_{rad,Z}/P_{in}$, to the total radiated power fraction, $f_{rad} = (P_{rad,D} + P_{rad,Z}) / P_{in} = f_Z + f_D$ in the confined edge region (Fig. 4a and b) and outer divertor region (Fig. 4c and d), with the results discussed below.

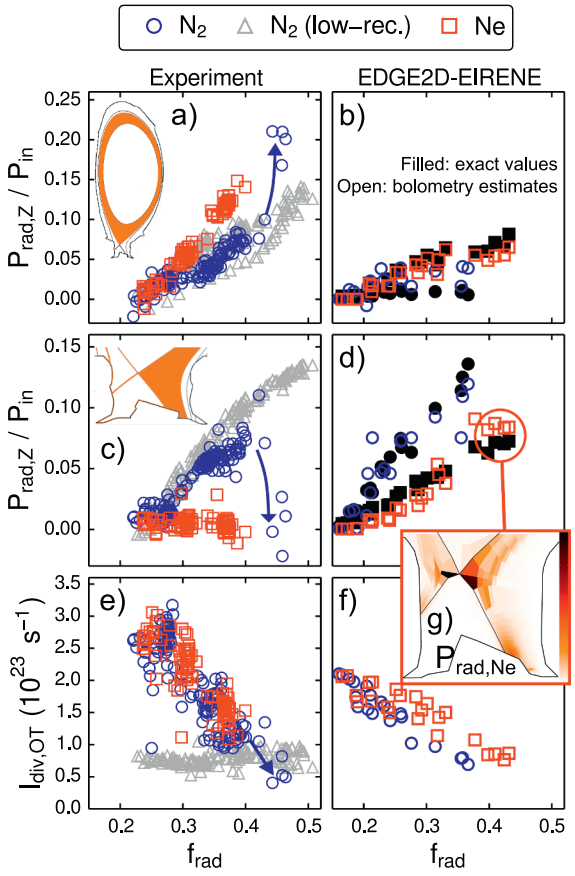

Fig. 4. Experiment and EDGE2D-EIRENE bolometry reconstruction macro-region estimates of the N (low and high recycling) and Ne (high recycling only) radiated power in the edge confined region, $0.9 \leq \rho_N \leq 1.0$, (a, b); the outer divertor region, (c, d), normalized by the input power P_{in}. Integrated ion current to the outer target, $I_{div,OT}$, (e, f). Blue arrows indicate transition to full detachment for the N high-recycling case. Filled symbols represent the exact $P_{rad,Z}$ values, whereas open symbols are the estimates from synthetic bolometry. (For interpretation of the references to color in this figure legend, the reader is referred to the web version of this article.)

3.1. Low-recycling vs. high-recycling N seeding scan

A consistent trend in f_N is observed in the outer divertor and edge confined regions comparing an existing L-mode low-recycling data set [36] to the high-recycling N seeding scan (Fig. 4a and c) until $f_{rad} \approx 0.4$, where a transition to pronounced detachment is observed in the high-recycling data set. Pronounced detachment is defined herein as the incursion of the radiation front from the outer divertor to inside the X-point confined region, as is evident from Fig. 4.a and c. The X-point radiation phase with N seeding is stable, as has been observed in previous studies at ASDEX Upgrade and JET [1,3,5,37], and in the present case results in only a modest f_{rad} increase from 0.4 to 0.45.

In the low-recycling scan $I_{div,OT}$ is approximately constant with f_{rad} (Fig. 4.e). Conversely, in the high-recycling unseeded reference $I_{div,OT}$ is already at the roll-over point and additional nitrogen seeding leads to an approximately linear decrease in $I_{div,OT}$ until pronounced detachment is reached with the corresponding transition to X-point radiation. To aid in the discussion of results, the degree of detachment in the present dataset is referred to as the reduction of $I_{div,OT}$ relative to the unseeded/low-seeding reference case at $f_{rad} \approx 0.25$. Although a more detailed comparison of the detachment evolution in the low and high-recycling N seeding scans was not possible due to limited outer target data for the low-recycling scan, a somewhat reduced seeding window in the high-recycling conditions is observed.

3.2. Comparison of N and Ne seeding scans in high-recycling

In contrast to the N seeding scan, discharges with Ne seeding showed no change in the outer divertor total radiated power, (i.e., f_{Ne}, $P_{rad,Ne} \approx 0$), as shown in Fig. 4.c. On the other hand, a steeper increase in f_{Ne} in the confined region was observed (Fig. 4.a), as well as a lower maximum $f_{rad} \approx 0.4$. With additional Ne seeding, the core plasma reached the radiative collapse limit and disrupted before full detachment could be accessed. The larger f_{Ne} contribution in the confined edge compared to f_N is also consistent with outer mid-plane T_e HRTS profiles, which show for the Ne cases a consistent reduction of few tens of eV in the region $0.9 \leq \rho_N \leq 1.0$. The reduced detachment window with Ne seeding is consistent with observations at higher P_{sep}/R (e.g., [3]), which indicate that in present day devices Ne is less applicable as a power exhaust seeding species from the perspective of plasma performance due to H-L back transitions at high Ne seeding rates and changes in pedestal transport of high-Z impurities such as tungsten, which may be mitigated to some extent with a sufficient increase in input power. Additionally, the strong de-enrichment (i.e., small divertor to the edge confined region f_Z ratio) observed with Ne seeding in L-mode is not indicative of the fraction of Ne radiation in the divertor in high P_{sep}/R conditions due to the strong temperature dependence of the radiative loss cooling function. For example, in JET-ILW seeded H-mode discharges with $P_{NBI} = 18$ MW [5], while the divertor radiation was observed to increase with Ne seeding in contrast to the present results, the ratio of radiation in the divertor to the main chamber was still 2–3 lower for Ne compared to N. Despite the differences in radiation distributions, both Ne and N seeding lead to a similar $I_{div,OT}$ vs. f_{rad} reduction, but with a greater degree of detachment obtained with N seeding at $f_{rad} \approx 0.35$ attributed to the local f_N contribution in the outer divertor. Hence, in the L-mode high-recycling data set detachment with N seeding proceeds via a reduction in P_{sep}, and thus P_{SOL}, in combination with local radiative dissipation above the target, whereas detachment with Ne seeding proceeds mainly via a reduction in P_{SOL}.

For consistency with the experiment data, the impurity radiation analysis for the N and Ne seeding scan in EDGE2D-EIRENE (Fig. 4b,d and f) was carried out using the same procedure as in experiment: (i) the numerical results were post-processed with synthetic bolometry reconstructions using the same set of bolometry chords as in experiment; (ii) the unseeded $P_{rad,D,ref}$ contribution was then subtracted from the total radiation, thus isolating the impurity radiation contribution

under the assumption that $P_{rad,D,ref}$ does not change appreciably, which is indeed the case in the simulations. The synthetic bolometry results are generally within 10–20% of the actual macro-region radiated powers, albeit with a larger overestimate of $P_{rad,N}$ in the confined region.

Relative to the experiment results, the high-recycling Ne and N simulation results show: (i) 25–30% lower f_{rad} in the unseeded reference case (i.e., shortfall in $P_{rad,D,ref}$); (ii) higher f_{Ne} in the divertor, and, conversely, lower f_{Ne} in the confined edge plasma; (iii) deeper detachment in N seeding at the same f_{rad} is reproduced due to enhanced f_N in the outer divertor compared to f_{Ne}; (iv) a ~30% difference in $I_{div,OT}$ at low f_{rad}. The apparent $P_{rad,D,ref}$ shortfall in EDGE2D-EIRENE is likely due to the unaccounted radiation contribution in the X-point region in the experiment $P_{rad,D,ref}$ estimates.

Since the synthetic bolometry f_N and f_{Ne} estimates faithfully reproduce the macro-region impurity radiation distribution between the outer divertor and confined edge region, the discrepancy between experiment and model results, and in particular with respect to Ne radiation, suggest that i) either transport effects are not fully captured in the model, or ii) that divertor conditions are markedly different. The correspondence in outer divertor leg T_e with increasing f_{rad}, as shown in Section 4, leads to consideration of transport effects as the more likely source of discrepancy between model and experiment. As shown in Fig. 4.g, the Ne radiation is highly concentrated in the SOL region near the X-point. Parallel T_e gradients along closed field lines in the confined region are not present in the EDGE2D simulations, even at the highest seeding rates, unlike in the no-drifts ASDEX-Upgrade cases with N seeding reported in [37]. Whether drift activation would promote the formation of X-point radiation inside the confined plasma and reconcile the observed discrepancies in the current data set remains an open question.

4. Spectroscopic analysis of impurity induced detachment

Fig. 5 compares experiment and model spectroscopically derived radial profiles including n_e, T_e, and Ly_α, D_α, and D_ϵ intensities for low seeding (experiment $f_{rad} \approx 0.26$), high seeding (experiment $f_{ra} \approx 0.38$) and fully detached (experiment $f_{rad} \approx 0.45$) cases corresponding to the upstream profiles shown in Fig. 2. The spectroscopic T_e estimates are bracketed by low and high T_e values since the photo-recombination continuum encodes a range of T_e estimates depending on which part of the Balmer continuum spectrum is sampled. Also shown are the spectroscopically inferred ionization rate profiles, as well as the outer target Langmuir probe profiles.

Low seeding

Although the spectroscopically derived T_e profiles in model and experiment are overall in good agreement (within 1 eV), the $T_{e,low}$ and $T_{e,high}$ estimates from experiment indicate a steeper gradient near the OSP. This feature is absent in the synthetic results. Closer to the X-point, there is again a large T_e gradient in experiment, which is not reproduced in the model. The concave shape of the T_e profiles originates from sampling the private flux region below the X-point where T_e is lower than in the common SOL along the outer leg approaching the X-point. Comparing the spectroscopically derived n_e profiles, a factor of three shortfall is observed for the low seeding simulation case. While both the Ly_α and D_α profiles peak at/near the OSP in the experiment and simulation results, a lower Ly_α peak intensity by a factor of three is observed in experiment. Integrating the Ly_α profiles over the outer target yields a ~30% lower total intensity in experiment. In post-processing the Ly_α and D_α profiles from EDGE2D-EIRENE simulations, only the atomic excitation and recombination components were included using ADAS *PEC* coefficients. If the large estimated contribution to D_α from D_2^+ dissociative recombination is included from EIRENE diagnostic output (see Section 2.2), then the profile peak is shifted outboard of the OSP, and increased by a factor of 3–4, which results in very poor agreement to experiment, and thus suggests that the D_2^+ contribution is overestimated by EIRENE. Regardless of the magnitude of the molecular contribution, the $n = 2$ excited state population is least affected by collisions with D_2^+, hence Ly_α is therefore the most direct measure of electron impact excitation/ionization for all recycling conditions. Work on the molecular contributions to the Lyman and Balmer series lines is ongoing (e.g., [38])

High seeding

At high f_{rad} with N seeding, $T_{e,low}$ at the OSP falls to 1–1.5 eV, and the profile flattens inboard of the OSP. The T_e profile evolution in the simulation is in very good agreement with experiment, within 0.5 eV. The shortfall of the simulated n_e profile is reduced, especially at the OSP. The Ly_α peak, which corresponds to the position of the ionization front, is shifted inboard, and roughly follows the $T_e = 2.5$–3 eV range. The D_α profile, on the other hand, remains peaked at the OSP in both experiment and model, which is attributed to a large recombination component. In experiment the contribution from D_2^+ dissociative recombination to the D_α profile is not resolved at present.

Pronounced detachment

A small ~2 cm inward shift of the OSP (i.e., away from the outer corner pump entrance) during a sweep for increased Langmuir probe resolution triggered a sudden transition to pronounced detachment with a stable X-point radiation regime. The transition is clearly visible from the incursion of the n_e front towards the X-point, along with a further incursion of the ionization front (Ly_α). The D_α secondary peak at $R = 2.61$ m, in combination with the n_e and Ly_α peaks in the same location, suggest a high electron density region in the vicinity of the X-point. This is also consistent with the flattened T_e profile extending to the X-point, indicating reduced neutral screening from the confined plasma, also corroborated in Fig. 2 by higher outer mid-plane edge density and lower temperature profiles for the high N seeding case.

For all simulation cases the D_ϵ intensity profile is dominated by the recombination component, thus validating its use for S_{rec} estimates (see Section 4.1). On the other hand, the recombination component contribution to Ly_α remains small, even at high f_{rad}, and is found in the simulations to contribute less than ~5% to the total outer divertor spectroscopic S_{iz} estimates.

As a consequence of Ly series opacity at the outer target with $\Theta_{2-1} \approx 0.1$, corrections to the ADAS *SCD* and *PEC* coefficients (see Section 2.2.2) informed by radial profiles measurements of Θ_{3-1} are used to modify the S_{iz} estimates derived from Ly_α emission (Fig. 5.a). The corrected profiles show significant increases in S_{iz} outboard of the OSP relative to S_{iz} estimates using the standard *SCD* and *PEC* coefficients. Applying the population escape factor methodology in ADAS collisional-radiative calculations, as in [27], gives rise to a modification of excited state population structure which results in an increase in the low-n population densities. The net effect on the Ly_α emission is roughly a 50% reduction in the peak intensity, which is consistent with the discrepancy evident in the Ly_α profiles between model and experiment. Opacity corrections for the entire seeding scan were based on only limited Θ_{3-1} measurements obtained from high-recycling unseeded L-mode conditions. Hence an implicit assumption in applying the opacity corrections is that the neutral density at the outer target does not change appreciably with incremental impurity seeding and constant D_2 fueling. This assumption can be tested, at least partially, by examining the neutral density evolution in the simulation data set, even though opacity effects in simulations are not captured. Fig. 6 shows the neutral deuterium density at the outer strike point, $n_{D,OSP}$, evolution with f_{rad}, which rises at low f_{rad} from 2–6 $\times 10^{19}\ m^{-3}$ and plateaus around $10^{20}\ m^{-3}$. The initial rise corresponds to a modest expansion of the high neutral density region from outboard of the OSP towards the OSP correlated with a decrease in

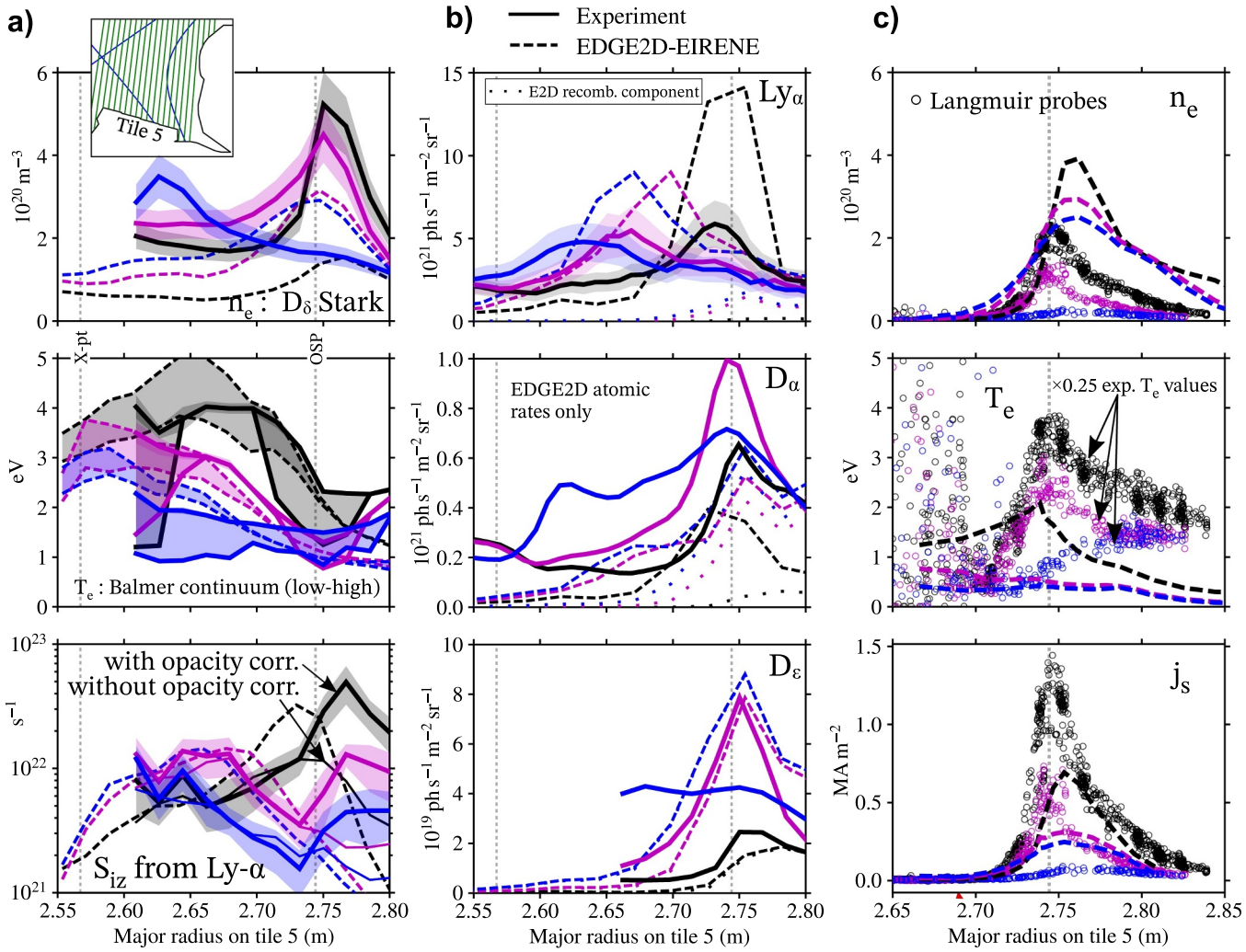

Fig. 5. Outer divertor radial profiles of (a) n_e and T_e, spectroscopically derived from the D_δ Stark broadening and the Balmer photo-recombination continuum, respectively, and S_{iz} derived from Ly_α; (b) Ly_α, D_α and D_ε intensity from experiment (full line) and EDGE2D-EIRENE post-processing (dashed line). (c) Outer target Langmuir probe n_e, T_e and saturation current, j_s, and the corresponding EDGE2D-EIRENE target values. Colors correspond to N seeding cases as in Fig. 2. (For interpretation of the references to color in this figure legend, the reader is referred to the web version of this article.)

$T_{e,OSP}$ (see Fig. 7). The assumption of relatively constant $n_{D,OSP}$ (within about a factor of 2) is thus reasonable, although additional opacity data at different N and Ne seeding levels would strengthen the above arguments. The synthetic spectroscopy estimate from Ly_α emission of the quantity $n_{D,OSP}\Delta L = 4\pi I_{2-1}/(n_e PEC^{exc}_{2-1})$, where ΔL is the effective height of the emission layer, is also shown. In practice the line-integration effects in spectroscopic estimates of $n_{e,OSP}$ and $T_{e,OSP}$, as well as reflections, can obscure the accurate determination of ΔL. The increase in $n_{D,OSP}\Delta L$ with f_{rad} suggests a broadening of ΔL with f_{rad}. A similar trend in both magnitude and evolution of $n_{D,OSP}$ ΔL is reproduced in experiment (Fig. 6), albeit with the requirement for employing the opacity corrected *PEC* coefficient. Although the $n_{D,OSP}$ ΔL comparison falls short of accurately estimating $n_{D,OSP}$ in experiment independent of the opacity corrections, the correspondence with the synthetic measurements suggests $n_{D,OSP} \sim 10^{19}$–10^{20} m^{-3}, which for $T_{e,OSP}$ = 1–2 eV gives a reabsorption mean-free path of a line-center Ly_α photon, λ_{mfp}, in the range 0.3–4 cm according to the scaling in [25]. With ΔL estimates in the range of a few cm at low f_{rad} to tens of cm at high f_{rad}, the relatively short λ_{mfp} reinforces the need for capturing opacity effects.

Comparing the outer target Langmuir probe (LP) (experiment) and on-target profiles (simulation) to the respective spectroscopic estimates of n_e and T_e in Fig. 5 shows that: i) in simulation, the line-integration effects on n_e are more pronounced at low f_{rad}, with about a factor of two underestimate from spectroscopy; ii) in simulation, the spectroscopic estimates of T_e are about 2 × higher than the actual target T_e; iii) in experiment, n_e (T_e) estimates from LPs are significantly lower (higher) compared to the spectroscopic estimates; and iv) the trend in the reduction of the ion saturation current profile is reproduced in the simulations, albeit with a lower peak by a factor of two, consistent with the differences in $I_{div,OT}$ shown in Fig. 4. The evolution of spectroscopic and LP estimates of $T_{e,OSP}$ and $n_{e,OSP}$ vs f_{rad} is also shown in Fig. 7. Taking the spectroscopic line-integration effects from simulation into account, there is good correspondence in spectroscopic $T_{e,OSP}$ between model and experiment, while a factor of 2–3 shortfall in the synthetic spectroscopy $n_{e,OSP}$ persists at lower f_{rad}. Experiment data for $f_{rad} < 0.26$ corresponds to a non-steady early phase of the discharges during which the D_2 fueling was still ramping up. The non-steady phase results in the observed initial $n_{e,OSP}$ rise that is not present in the simulations. Nevertheless, this early phase expands the range for comparison of LPs and spectroscopy and has little impact on the trends reported in Section 3 with respect to f_{rad}. Interpretation of the LP T_e results was carried out using a 4-parameter model [39] which is then used to constrain an expression for n_e according to the proportionality $n_e \propto T_e^{0.5}$. LP overestimates of T_e in high-recycling conditions, as shown

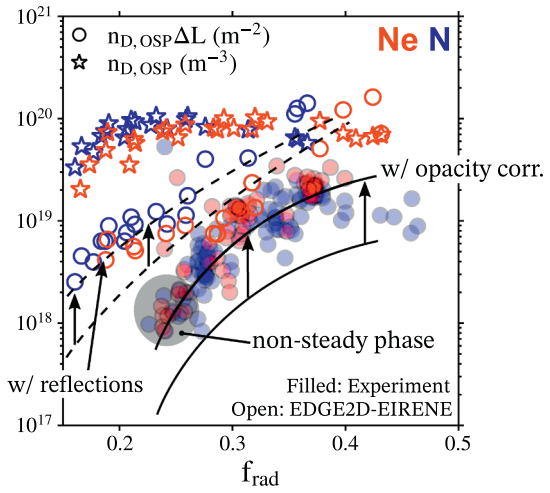

Fig. 6. EDGE2D-EIRENE deuterium atomic density at the OSP, $n_{D,OSP}$, and OSP spectroscopic estimates of $n_{D,OSP}\Delta L$ from EDGE2D-EIRENE (open) and experiment (filled). Arrows and trend lines indicate impact of reflections on synthetic spectroscopy estimates and the impact of opacity corrections on experiment estimates. (For interpretation of the references to color in this figure legend, the reader is referred to the web version of this article.)

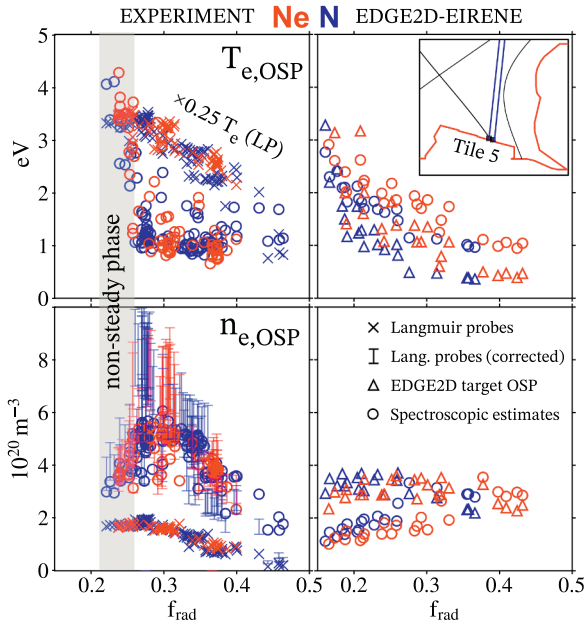

Fig. 7. Spectroscopically derived OSP n_e and T_e and corresponding OSP target values (EDGE2D-EIRENE) and Langmuir probe values (experiment). The corrected Langmuir probe n_e values were obtained by replacing the LP T_e with the spectroscopically derived values in the 4-parameter fit model ($n_e \propto T_e^{-0.5}$). (For interpretation of the references to color in this figure legend, the reader is referred to the web version of this article.)

in Figs. 5 and 7, are well documented (e.g., [40,41]). By replacing the LP derived $T_{e,OSP}$ with the spectroscopic estimates, and using the above proportionality, the LP corrected $n_{e,OSP}$ values in Fig. 7 are obtained, with the error bars accounting for a factor of two line-integration effect on spectroscopic $T_{e,OSP}$ estimates, as suggested by the synthetic spectroscopy. Both the magnitude and trend are recovered in the corrected LP estimates relative to the spectroscopic estimates of $n_{e,OSP}$,. If the line-integration factor of two obtained in synthetic spectroscopic $n_{e,OSP}$ estimates is carried over to the experiment results, then the actual target density peak is in the range 6–10 $\times$ 10^{20} m^{-3}. The $n_{e,OSP}$ shortfall at low f_{rad} in the simulations is not reconciled in the present study. A factor of two increase in the target densities as a result of opacity effects has been previously reported based on a numerical simulation study [42] using the EIRENE photon transport module in JET-carbon vertical target configuration. The results of the present study therefore motivate extending the present N and Ne seeding scan with more sophisticated photon transport modeling.

4.1. Particle balance

Since the recycled flux consists of both atomic and molecular neutrals, the ionization source rate includes contributions to the production of D^+ ions born out of atom-plasma interactions (electron impact excitation and ionization) as well as molecule-plasma interactions (D_2^+ and D_2 collisions with plasma, see [21] for an overview). In the high-recycling seeded EDGE2D-EIRENE cases examined, the molecule-plasma contributions to the production of D^+ (including molecular assisted dissociation, MAD, and ionization, MAI) are roughly 10–25% of the magnitude of the total atomic ionization rate, whereas the molecular assisted recombination (MAR) rate of D^+ removal is of similar magnitude, and hence, largely cancels out D^+ production via molecular interactions. The remaining D^+ volumetric source is therefore dominated by atomic ionization and the volumetric D^+ sink by three-body recombination. The balance between the atom-plasma sources and sinks (Fig. 8.a, filled markers) is in good agreement with $I_{div,OT}$, indicating that the net inflows and outflows of D^+ into the outer divertor volume are small compared to the volumetric source and sink terms due to outer target recycling. Thus the particle balance in the outer divertor is well approximated by the closed box description, such that $I_{div,OT} \approx S_{iz} - S_{rec}$.

The spectroscopically derived S_{rec} inferred from D_ε emission is within 25% of the actual macro-region values from the EDGE2D-EIRENE output over the entire f_{rad} range (Fig. 8.a). However, the spectroscopically derived S_{iz} inferred from Ly_α emission is underestimated by up to almost a factor of two at high f_{rad}. The cause of the discrepancy is primarily due to two effects, namely: i) a spatial separation between the bright Ly_α region of emission which is at higher T_e compared to the photo-recombination emission from which T_e is inferred; and ii) to a lesser extent, an overall decrease in the T_e profile due to the influence of reflections (see Fig. 3). The spectroscopically derived particle balance is, in general, more robust at lower f_{rad}, for which the spectroscopically derived T_e estimates are more representative of the dominant Ly_α emitting region.

Following the same interpretation procedure in experiment, and using, in the first instance, the unmodified ADAS *SCD, ACD* and *PEC* coefficients, the spectroscopically inferred S_{rec} and S_{iz} estimates (Fig. 8.b) show that: i) volume recombination is not a significant D^+ sink over the entire f_{rad} range; and ii) a significant (up to 3 $\times$) D^+ source deficit is evident even at low f_{rad} where line-integration effects are small according to the synthetic spectroscopy results. Hence, the D^+ source deficit is much larger than the expected shortfall due to line-integration effects. Two additional mechanisms are considered for elucidating the S_{iz} shortfall: opacity corrections and possible additional contributions to D^+ sources from molecule-plasma interactions not captured in the spectroscopic estimates.

Estimates of S_{iz} obtained using the opacity corrected ADAS coefficients within the uncertainty range of the $\Theta_{3\text{-}1}$ measurements (giving $0.05 \leq \Theta_{2\text{-}1} \leq 0.1$) do recover the S_{iz} deficit relative to $I_{div,OT}$ (Fig. 8.c). Likewise, S_{rec} is reduced by about a factor of two compared to the uncorrected values. It's important to highlight again the fact that opacity corrections in the spectroscopic interpretation do not directly provide any information about the influence of opacity on the recycling dynamics. In other words, the S_{iz} deficit obtained without opacity corrections does not imply that Ly series opacity leads to a 3 $\times$ increase in the total ionization rate. Nevertheless, the 30% difference in $I_{div,OT}$ at low f_{rad} between model and experiment suggests that opacity could play a significant role in mediating the magnitude and evolution of the D^+

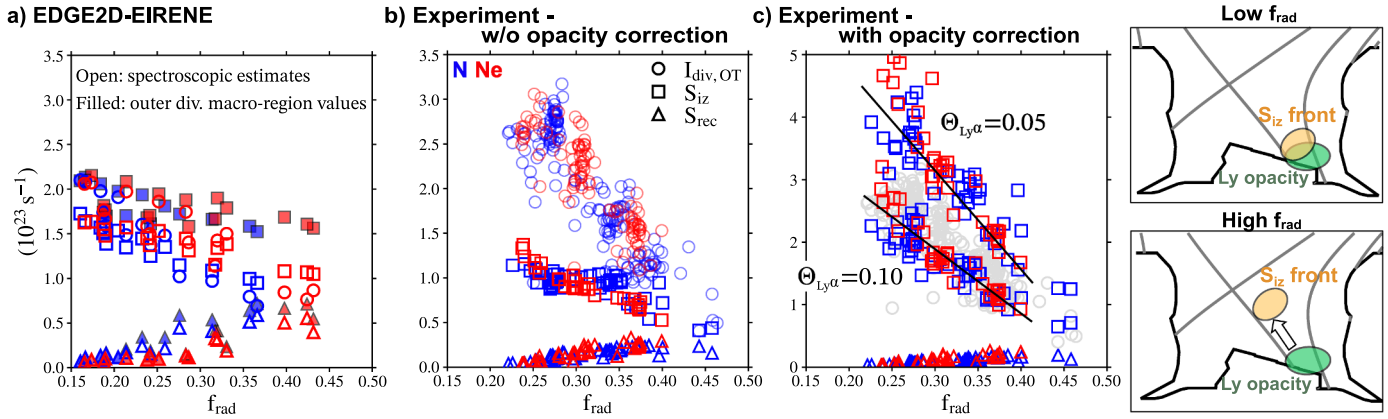

Fig. 8. D^+ particle balance in the outer divertor: a) EDGE2D-EIRENE results - filled symbols are the macro-region exact S_{iz} and S_{rec} values, open triangles (S_{iz}) and squares (S_{iz}) are the spectroscopic estimates, and open circles correspond to the outer target ion flux ($I_{div,OT}$); b) experiment spectroscopic S_{iz} and S_{rec} estimates without opacity corrections and c) with upper and lower range of opacity corrections. (For interpretation of the references to color in this figure legend, the reader is referred to the web version of this article.)

source term in the L-mode conditions examined. Within the detachment description given by Eq. (1), the impact of opacity is to lower the ionization cost E_{iz}, which is reflected in the population structure changes that lead to modification of the ADAS *SCD* and *PEC* coefficients. In addition, 2D ionization front dynamics could also play a role, as follows. At low f_{rad} the overlap of the ionization front and high opacity region near the OSP gives rise to enhanced ionization leading to higher $I_{div,OT}$ and potentially higher $n_{e,OSP}$. A similar effect has been shown in [43] using the EIRENE photon transport module to assess the role of opacity in JET and ITER exhaust scenarios; however, in this study the increase in target density also led to an enhancement in volume recombination, which is not observed in the present data set where the recombination sink is small. With additional seeding, the incursion of the ionization front away from the region of high opacity leads to a more rapid S_{iz} decrease compared to the simulations due to increasing E_{iz} at the position of the ionization front (see illustration in Fig. 8). Additional photon transport modeling is needed to test this hypothesis and compare the recycling dynamics in the present horizontal target configuration to the vertical target scenarios considered in [43].

Alternatively, the measured S_{iz} deficit could also be recovered to some degree, and independent of opacity considerations, by the D^+ source from molecule-plasma interactions. Previous studies in carbon wall machines (e.g., [24,44]) do indicate comparable D and D_2 influx from recycling at the first wall, suggesting that the molecular dissociation processes are important. However, the net-neutral D^+ balance between MAD, MAI and MAR observed in the EDGE2D-EIRENE simulations does not support a large net D+ source arising from molecular processes that could explain the observed S_{iz} deficit. Experimental verification of the molecular contribution is challenging in the JET-ILW environment due to possible tungsten surface effects, which invalidate previous techniques for estimating the inverse photon efficiency for the D^+ source from D_2 Fulcher-α spectroscopy [45]. Efforts to address the tungsten surface effects on the Fulcher-α population distribution are ongoing.

5. Summary

L-mode Ne and N seeded discharges in the outer horizontal target configuration have been analyzed employing a combination of spectroscopic and bolometric measurements in experiment with a complementary synthetic spectroscopy framework for post-processing numerical results from EDGE2D-EIRENE.

For the conditions examined, the dominant Ne radiation contribution in experiment is in the confined edge region, whereas N radiation is split more evenly between the confined edge and outer divertor. While the synthetic bolometry analysis in the simulation data set reproduces the N radiation magnitude and evolution in the outer divertor, a shortfall in both N and Ne radiation inside the X-point confined region is observed. Additionally, significant Ne radiation in the outer divertor is present in the simulations, whereas in experiment virtually no Ne radiation is measured in the outer divertor for the low input power and high-recycling conditions examined. The quality of the bolometry reconstructions has been shown through synthetic measurements to be sufficient for resolving the macro-region radiation distribution between the edge confined X-point region and outer divertor. Given the correspondence in the outer divertor T_e evolution between model and experiment, the radiation distribution discrepancies are likely due to transport effects, and not due to mismatched plasma conditions. The influence of drifts on the impurity radiation distribution at high seeding rates was not captured in the simulations, and may ameliorate the observed discrepancies, especially in view of the N and Ne radiation being localized in very close proximity to the X-point region. Overall, a larger reduction in the outer target ion flux is obtained with N seeding due to the local radiated power dissipation in the outer divertor which was not present with Ne in the low P_{sep}/R conditions examined.

Using the spectroscopic framework in both experiment and model to infer radial profiles of n_e and T_e showed that at low radiative fractions the outer target electron density in simulations is about a factor of two lower than in experiment. A detailed analysis of spectroscopic line-integration effects, reflections, and corrections to experiment Langmuir probe measurements further support this observation. In addition, the peak Ly_α emission in experiment was observed to be almost 3 × lower than in the simulations for the same outer target T_e. Including opacity corrections in ADAS collisional-radiative population modeling is shown to modify the neutral deuterium excited population structure such that a factor of two decrease in the measured peak Ly_α emission is to be expected compared to the simulations in which opacity effects are not captured. Moreover, it is likely that strong Ly photon reabsorption increases the target electron density due to an enhanced ionization rate, which could also reconcile the observed density shortfall in simulations and is consistent with previous photon transport modeling.

Synthetic spectroscopy estimates of the ionization and recombination rates in the simulations are shown to recover the particle balance, albeit with more pronounced line-integration effects on ionization rate estimates at high radiative fractions. In the N and Ne seeding scan simulations, a combination of a reduction in ionization rate and an increase in recombination rate are observed with increasing radiative fraction. On the other hand, in experiment, the recombination rate is observed to be small even at high radiative fractions. Only when opacity corrections are included in the experiment ionization rate estimate

does the magnitude and rate of decrease correspond to the reduction in the target ion flux with increasing seeding. In high-recycling conditions with N and Ne seeding, it is concluded that the plasma flux to the outer target is reduced primarily by a reduction in the ionization source rate. Additional dynamics due to the interplay of the opacity region at the outer target and the inward shift of the ionization front with increased impurity seeding gives rise to i) a 50% higher total ionization source rate at low radiative fraction (3×10^{23} vs 2×10^{23} s^{-1}) compared to simulations; and ii) a steeper rate of decrease in the ionization source rate (and hence the outer target ion flux) compared to simulations.

The synthetic spectroscopy framework offers strategies for including approximate opacity corrections in the interpretation of ionization and recombination rate estimates as well as Lyman and Balmer series line intensities. On the other hand, quantifying the influence of opacity on divertor dynamics demands sophisticated photon transport modeling. Therefore, it is recommended that the impurity seeding simulations be extended to include the latest version of the EIRENE photon transport module to further examine the opacity effect on the balance between ionization and recombination and the evolution of the 2D ionization front and impurity radiation distribution.

Acknowledgements

This work has been carried out within the framework of the EUROfusion Consortium and has received funding from the Euratom research and training programme 2014–2018 under grant agreement no 633053. The views and opinions expressed herein do not necessarily reflect those of the European Commission. This work is also supported, in part, by the US DOE under Contract no. DE-AC05-00OR22725 with UT-Battelle, LLC.

References

[1] M. Wischmeier, J. Nucl. Mater. 463 (2015) 22–29, https://doi.org/10.1016/j.jnucmat.2014.12.078.
[2] A.S. Kukushkin, et al., J. Nucl. Mater. 438 (2013) S203–S207, https://doi.org/10.1016/J.JNUCMAT.2013.01.027.
[3] M. Bernert, et al., Nucl. Mater. Energy 12 (2017) 111–118, https://doi.org/10.1016/j.nme.2016.12.029.
[4] A. Kallenbach, et al., Nucl. Fusion (2015) 55, https://doi.org/10.1088/0029-5515/55/5/053026.
[5] A. Huber, et al., 41st EPS Conf. Plasma Phys. 2012, pp. 5–8.
[6] A.R. Field, et al., Plasma Phys. Control. Fusion 59 (2017) 095003, , https://doi.org/10.1088/1361-6587/aa764c.
[7] M.N.A. Beurskens, et al., Plasma Phys. Control. Fusion 55 (2013) 124043, , https://doi.org/10.1088/0741-3335/55/12/124043.
[8] A. Kallenbach, et al., Plasma Phys. Control. Fusion 38 (1996) 2097–2112, https://doi.org/10.1088/0741-3335/38/12/005.
[9] J. Neuhauser, et al., Plasma Phys. Control. Fusion 37 (1995) A37–A51, https://doi.org/10.1088/0741-3335/37/11A/003.
[10] S.I. Krasheninnikov, et al., Phys. Plasmas 23 (2016) 55602, , https://doi.org/10.1063/1.4948273.
[11] R, C.G Simonini, et al., Contrib. Plasma Phys. 34 (2006) 368–373.
[12] D. Reiter, J. Nucl. Mater. 196–198 (1992) 80–89, https://doi.org/10.1016/S0022-3115(06)80014-0.
[13] S. Wiesen, EDGE2D/EIRENE code interface report, 2006. http://www.eirene.de/e2deir_report_30jun06.pdf.
[14] B.A. Lomanowski, et al., Nucl. Fusion 55 (2015) 123028, , https://doi.org/10.1088/0029-5515/55/12/123028.
[15] D. Lumma, et al., Phys. Plasmas 4 (1997) 2555–2566, https://doi.org/10.1063/1.872234.
[16] A. Meigs, et al., Rev. Sci. Instrum. 81 (2010) 10E532, https://doi.org/10.1063/1.3502322.
[17] B.A. Lomanowski, et al., Rev. Sci. Instrum. 85 (2014) 0–5, https://doi.org/10.1063/1.4893426.
[18] H.P. Summers, et al., Plasma Phys. Control. Fusion 48 (2006) 263–293, https://doi.org/10.1088/0741-3335/48/2/007.
[19] K.D. Lawson, et al., Rev. Sci. Instrum. 83 (2012) 2012–2015, https://doi.org/10.1063/1.4745213.
[20] D. Reiter, EIRENE Manual, 2017. http://www.eirene.de/html/manual.html.
[21] D. Wünderlich, et al., Atoms 4 (4) (2016), https://doi.org/10.3390/atoms4040026.
[22] M. Groth, et al., Nucl. Mater. Energy 19 (2019) 211–217.
[23] J.L. Terry, et al., Phys. Plasmas 5 (1998) 1759–1766, https://doi.org/10.1063/1.872845.
[24] E.M. Hollmann, et al., Plasma Phys. Control. Fusion 48 (2006) 1165–1180, https://doi.org/10.1088/0741-3335/48/8/009.
[25] A. Loarte, et al., Nucl. Fusion (2007) 47, https://doi.org/10.1088/0029-5515/47/6/S04.
[26] K. Behringer, U. Fantz, et al., New J. Phys. (2000) 2, https://doi.org/10.1088/1367-2630/2/1/323.
[27] C.F. Maggi, et al., J. Nucl. Mater. 266 (1999) 867–872, https://doi.org/10.1016/S0022-3115(98)00845-9.
[28] M. Groth, et al., Nucl. Fusion (2013) 53, https://doi.org/10.1088/0029-5515/53/9/093016.
[29] adaslib/continuo, (n.d.). http://www.adas.ac.uk/sr/continuo.php (Accessed July 16, 2018).
[30] V. Kotov, et al., Plasma Phys. Control. Fusion (2008) 50, https://doi.org/10.1088/0741-3335/50/10/105012.
[31] D. Reiter, et al., J. Nucl. Mater. 313–316 (2003) 845–851, https://doi.org/10.1016/S0022-3115(02)01573-8.
[32] M. Carr, et al., 44th EPS Conf. Plasma Phys. 2017.
[33] M. Carr, A. Meakins, Raysect Python Raytracing Package (Version v0.4.0), (2017 December 11), (n.d.). doi:http://doi.org/10.5281/zenodo.1205064.
[34] T. Asdex Upgrade Team, et al., Plasma Phys. Control. Fusion (2017) 59, https://doi.org/10.1088/1361-6587/59/3/035003.
[35] A.E. Jaervinen, et al., Nucl. Mater. Energy 19 (2018) 230–238.
[36] L. Aho-Mantila, et al., J. Nucl. Mater. (2013) 438, https://doi.org/10.1016/j.jnucmat.2013.01.059.
[37] F. Reimold, et al., J. Nucl. Mater. 463 (2015) 128–134, https://doi.org/10.1016/j.jnucmat.2014.12.019.
[38] M. Groth, et al., Nucl. Mater. Energy. 19 (2019) 211–217, https://doi.org/10.1016/J.NME.2019.02.035.
[39] J.P. Gunn, et al., Rev. Sci. Instrum. 66 (1995) 154, https://doi.org/10.1063/1.1145249.
[40] J. Horacek, et al., J. Nucl. Mater. 313–316 (2003) 931–935, https://doi.org/10.1016/S0022-3115(02)01479-4.
[41] P.C. Stangeby, Plasma Phys. Control. Fusion. 37 (1995) 1031–1037, https://doi.org/10.1088/0741-3335/37/9/008.
[42] V. Kotov, et al., 33rd EPS Conference on Plasma Phys. Rome, Vol. 30I 2006 ECA, P-1.128.
[43] V. Kotov et al., Numerical study of the ITER divertor plasma with the B2-EIRENE code package, report accessed online http://eirene.de/kotov_solps42_report.pdf (2007).
[44] S. Brezinsek, et al., J. Nucl. Mater. 313–316 (2003) 967–971, https://doi.org/10.1016/S0022-3115(02)01421-6.
[45] G. Sergienko, et al., J. Nucl. Mater. 438 (2013) S1100–S1103, https://doi.org/10.1016/j.jnucmat.2013.01.242.